Continental Shelf Research
July 2017, Volume 144, Pages 98-111
http://dx.doi.org/10.1016/j.csr.2017.06.024
http://archimer.ifremer.fr/doc/00391/50258/

Investigating Rhône River plume (Gulf of Lions, France) dynamics using metrics analysis from the MERIS 300m Ocean Color archive (2002 − 2012)

Gangloff Aurélien [1, *], Verney Romaric [1], Doxaran David [2], Ody Anouck [2], Estournel Claude [3, 4]

[1] IFREMER, Laboratoire DYNECO/DHYSED, PB70 29280 Plouzane, France
[2] Observatoire Océanologique, Laboratoire d'Océanographie de Villefranche, UMR 7093 – CNRS/UPMC, 181 Chemin du Lazaret, 06230 Villefranche sur Mer, France
[3] Laboratoire d'Aérologie, CNRS et Université Paul Sabatier, 14, Avenue Edouard Belin, 31400 Toulouse, France

* Corresponding author : Aurélien Gangloff, email address : aurelien.gangloff@ifremer.fr

Abstract :

In coastal environments, river plumes are major transport mechanisms for particulate matter, nutriments and pollutants. Ocean colour satellite imagery is a valuable tool to explore river turbid plume characteristics, providing observations at high temporal and spatial resolutions of suspended particulate matter (SPM) concentration over a long time period, covering a wide range of hydro-meteorological conditions. We propose here to use the MERIS-FR (300 m) Ocean Colour archive (2002–2012) in order to investigate Rhône River turbid plume patterns generated by the two main forcings acting on the north-eastern part of the Gulf of Lions (France): wind and river freshwater discharge. Results are exposed considering plume metrics (area of extension, south-east-westernmost points, shape, centroid, SPM concentrations) extracted from satellite data using an automated image-processing tool. Rhône River turbid plume SPM concentrations and area of extension are shown to be mainly driven by the river outflow while wind direction acts on its shape and orientation. This paper also presents the region of influence of the Rhône River turbid plume over monthly and annual periods, and highlights its interannual variability.

Highlights

► A new method to extract plume metrics from ocean color satellite images is proposed. ► Use of innovative plume metrics such as centroids and schematic shape (skeleton). ► Analysis of the MERIS-300m database covering the 2002–2012 period. ► Grand Rhone River turbid plume metrics are highly correlated to river discharge. ► Wind regime (Onshore/offshore) drives plume patterns.

Keywords : river plume metrics, sediment dynamics, MERIS, ocean color data, suspended particulate matter, Gulf of Lions

1 Introduction

Understanding particulate matter dynamics over continental margins is a challenging issue for environmental purposes as fine particles are vectors of pollutants such as heavy metals or radionuclides. In the North-Eastern (NE) part of the Gulf of Lions (GoL), located in the North- Western (NW) part of the Mediterranean Sea (Fig. 1), the Rhône River is the main source of sediments (Bourrin and Durrieu de Madron, 2006). These particles can be trapped within the

prodelta located just downstream from the river mouth (Radakovitch et al., 1999; Roussiez et al., 2005) or advected along the shelf as suspended particulate matter (SPM), directly within the river plume or indirectly, after wave-induced resuspension events, occurring mainly during winter storms (Dufois et al., 2014). This work focuses on the SPM advected directly from the Rhône River mouth into the GoL through the plume dynamics.

The Rhône is one of the major rivers of the Mediterranean basin, the most important in the GoL, flowing from Swiss Alps (Lac Leman) to the Mediterranean Sea, where it divides in two branches, about 50 km upstream the main river mouth: the Grand Rhône and the Petit Rhône (see Fig. 1). The river drains continental waters over a 97800 km^2 catchment area, covering different climatic zones such as alpine, oceanic and Mediterranean ones (Maillet et al., 2006). The mean annual discharge of the Rhône River is 1700 $m^3.s^{-1}$, and about 90 % (~ 1500 $m^3.s^{-1}$) is distributed to the GoL *via* the Grand Rhône (Fanget et al., 2013). Annual, decennial, centennial and millennial floods water discharges for Rhône River are of about 5000, 8400, 11300 and 14100 $m^3.s^{-1}$, respectively (Maillet et al., 2006), leading to about 4500, 7600, 10200 and 12700 $m^3.s^{-1}$ for the Grand Rhône River, respectively. For the following study, we chose to focus on the Grand Rhône River plume only.

The Rhône River plume dynamics has been studied for several years through observations like sea temperature monitoring with TIROS-N satellite database by Demarcq and Wald (1984), showing that the plume response time is short, about 5 h for average river discharges (Q_w - typically around 1500 $m^3.s^{-1}$) and increases with river outflow, above 24 h for river discharge values of 4350 $m^3.s^{-1}$ for instance. They also highlighted that the plume is clearly deflected on the right side of the wind, with an average angle of deflection of 50°. However, the thermal plume depth sensed by AVHRR is very thin (O(10μm)) compared to turbid plume depth (O(0.1m) to O(1m)), so results are not fully comparable, but provide complementary knowledge about the near surface dynamics. Forget et al. (1990) also showed, through VHF radar analysis, that for low river discharges (500 to 800 $m^3.s^{-1}$) and calm wind conditions, summer breezes (< 5 $m.s^{-1}$) are able to push the plume front toward the river mouth over a distance of about 10 km in a few hours. Broche et al. (1998), relying on field and VHF data measurements, reported that flow intensity variations have a weak influence on the plume's shape but act on its vertical thickness and its internal velocity variations. They also highlighted that strong western winds can deflect the plume eastward within a few hours. The Rhône River plume dynamics was also investigated through numerical modelling. Estournel et al. (1997) showed that the river plume is highly sensitive to wind, yet two types of plumes were brought to the fore, associated to the two predominant wind regimes in the climate of the Gulf of Lions. The typical plume shapes observed are the following: detached from the coast and orientated southwestward, or thin and running along the coast, orientated westward, for northern and southeastern winds, respectively. Marsaleix et al. (1998) added that for simulations forced by northwestern winds of different intensities, the seaward deflection is significant for wind velocities higher than 7 $m.s^{-1}$. These studies focused on freshwater river plume dynamics and not on the turbid plume one, which could not necessarily behave identically. Also, they focused on short time periods (daily to

monthly analysis). In the present paper, we will investigate the turbid plume dynamics over a 10 years database, allowing event to decennial analysis. Recent works on the studied area attempted to characterize the turbid plume. For high river discharge (~ 4000 $m^3.s^{-1}$) and calm conditions (northwestern wind with velocity < 3 $m.s^{-1}$), Many et al. (2016) observed a plume expanding up to 30 km off the coast, with a thickness decreasing seaward from 20 m to 5 m, as well as for its depth-averaged SPM concentration, decreasing from 15 down to 5 $mg.l^{-1}$. Using satellite ocean colour data, Lorthiois et al. (2012) showed that the duration of a flood event has an influence on the turbid plume vertical thickness. Their results revealed that during a strong river discharge event (15 consecutive days with Q_w > 2000 $m^3.s^{-1}$), the plume reached a thickness of ~ 5 m, which was not the case for a shorter event (3 consecutive days with Q_w > 2000 $m^3.s^{-1}$), where the plume thickness was of ~ 1 m.

In the present paper, we propose to investigate the Rhône River turbid plume patterns and dynamics from the decennial scale down to the event scale, in relation with the main forcings prevailing on the area (Fig. 1). These forcings are: (i) the strong continental winds called Mistral (from the North) and Tramontane (from the North-West), which curl drives the coastal currents direction (Estournel et al., 2003); (ii) the Rhône River discharge and (iii) the general circulation following the slope of the GoL shelf, called the Northern Curent (Millot, 1990), south the area of interest. The study area, which is located on the inner shelf of the GoL, is a wave-dominated area (Dufois et al., 2008) with low tidal range of about 0.3 m (Fanget et al., 2013).

Investigating turbid plume patterns and their relation with forcings requires to have a long time-period dataset, representative of the meteorological/hydrological conditions. Satellite imagery has proven to be a valuable tool to assess turbidity or SPM concentration from ocean colour data in estuaries (Hudson et al., 2016) and coastal zones such as the North Sea (Gohin, 2011; Nechad et al., 2010), the Bay of Biscay (Gohin et al., 2005), the Danube River (Constantin et al., 2016; Güttler et al., 2013), the Adour River (Petus et al., 2010; Petus et al., 2014), the Gironde estuary (Doxaran et al., 2006; Doxaran et al., 2009) or the Gulf of Lions (Lorthiois et al., 2012; Ody et al., 2016) for instance. Ocean colour satellite imagery can be used to study turbid plume metrics such as its extension area in relation with hydrological and meteorological forcings, as it has already been done for the Mississippi River plume (Walker, 1996; Walker et al., 2005), the Adour River plume (Petus et al., 2014) or the Ebro River plume (Fernández-Nóvoa et al., 2015).

Based on the 10-year MERIS-300m archive, the main objectives of this study are:

1. to report the inter-annual and seasonal variability of the Rhône River turbid plume in terms of area of extension, averaged SPM concentration and maximum SPM concentration;
2. to highlight turbid plume patterns in response to typical forcings acting on the study area, exploring various metrics, such as its area of extension, its centroid, its shape or its extreme points (southernmost, westernmost and easternmost).

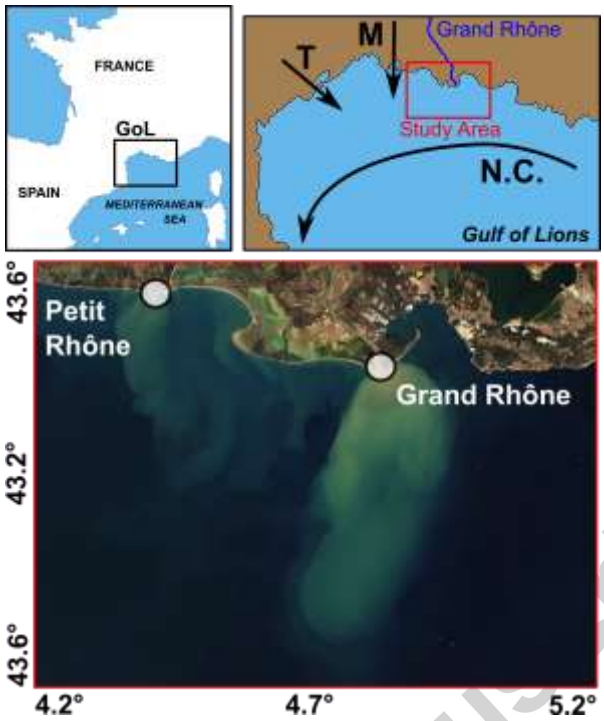

Figure 1: RGB (Landsat 8 OLI image recorded on 23rd february 2014) map of the study area and geolocalisation of Petit Rhône and Grand Rhône river mouths. Northern Current (N.C.), Mistral (M) and Tramontane (T) winds are indicated by black arrows on the GoL map on the top-right illustration.

2 Materials and methods

2.1 MERIS-300m database

Entering the water, solar irradiance interacts with its constituents and a part of the signal is scattered backward out of the water column. Ocean colour sensors measure the spectral characteristics of this backscattered signal. This water-leaving radiance (in $W.m^{-2}.nm^{-1}.sr^{-1}$) can be normalized by the downward irradiance (in $W.m^{-2}.nm^{-1}$) just above the surface at different wavelengths. This normalized radiance is called the remote sensing reflectance (R_{rs}, in sr^{-1}) and can be expressed in terms of inherent optical properties (IOPs), such as the total backscattering and absorption coefficients, depending on the nature and concentration of a substance. After atmospheric correction processes, it is then possible to retrieve the concentration of substances in the surface water layer sensed by ocean colour sensors (optical depth). In the present study, the medium-spectral resolution imaging spectrometer MERIS-300m seawater reflectance data was used to evaluate SPM concentrations on the study area (Fig. 1). Archived data are available from 2002 to 2012 with a global coverage every 3 days.

Data was collected *via* the online GIS COOC data portal (http://kalicotier.gis-cooc.org/), providing two reflectance products of MERIS Full Resolution. The first one is based on the atmospheric correction processor MEGS8.1 (third reprocessing of the MERIS Ground Segment prototype processor), standard processor for the MERIS sensor (Müller et al., 2015) which uses a

neural network algorithm applied for atmospheric correction specific for the retrieval of case2 water constituents (Doerffer and Schiller, 2007). The second one is based on the SAABIO (Semi-Analytical Atmospheric and Bio-Optical) processor (Gernez et al., 2014), using MEGS8.1 with a different bright pixel atmospheric correction and without the case2 regional neural network for computing SPM concentration.

The standard SPM product, available from the MEGS8.1 neural network (Doerffer and Schiller, 2007) was tested, as well as three other regional algorithms identified hereafter as SPM1, SPM2 and SPM3. SPM1 and SPM2 were derived from field data collected during the TUCPA (2014) and the PLUMRHO (2015) experiments, as well as SPM3, following the formulation of the generic model developed by Nechad et al. (2010). These algorithms use the *Rrs* at 620 nm and/or 655 nm and are the following:

a linear regression, associating SPM concentration (mg.l^{-1}) to *Rrs* in the 665 nm band (Ody et al., 2016),

$$SPM1 = 1515 \times Rrs_{665} - 0.088$$

another linear regression, using the mean of the 665 nm and the 620 nm bands,

$$SPM2 = 1420 \times \frac{Rrs_{620} + Rrs_{665}}{2} - 0.12$$

and a non-linear regression, derived from the generic model of Nechad et al. (2010) and using the 665 nm band,

$$SPM3 = \frac{A \times \rho_{665}}{1 - \frac{\rho_{665}}{C}} + B$$

where $\rho_{665} = \pi Rrs_{665}$ is the water leaving reflectance at 665 nm, coefficient C = 0.1728 was theoretically calculated for the MERIS 665 nm band in Nechad et al. (2010), and coefficients A = 213 and B = - 0.0785 were optimized for our region of interest considering data collected during the two field experiments mentioned above.

The performances of the standard SPM product and the regional SPM algorithms were evaluated using SPM matchups. These matchups are *in situ* measurements close in time (< 6 h) and space (nearest pixel) to the satellite acquisition and were obtained during field campaigns from 2010 to 2012 (Table 1). The same sampling and filtering protocol was used for each campaign. They cover a range of SPM concentration from 0.8 mg.l^{-1} to 32 mg.l^{-1}, with a mean of 8.2 mg.l^{-1}. The MEGS8.1 standard product showed very good performances with a mean relative error ε_r of 40.0 %, a R^2 of 79.4 and root mean square errors *RMSE* for SPM concentrations ≤ 10 mg.l^{-1} and > 10 mg.l^{-1} of 2.56 and 6.45 mg.l^{-1}, respectively. The semi-empirical relation described by Nechad et al. (2010) for the SAABIO product also showed good statistical results with a ε_r of 37.0 %, a R^2 of 79.3 % and *RMSE* for SPM concentrations ≤ 10 mg.l^{-1} and > 10 mg.l^{-1} of 2.02 and 6.52 mg.l^{-1}, respectively. Both algorithm results were close and, in order to minimize data processing, the standard SPM product was chosen for this study.

Table 1: Number of matchups (N), ε_r (%), *RMSE* (mg.l^{-1}) and R^2 coefficients for tested algorithms. The selected product (Doeffer & Schiller, 2007) is highlighted in green.

Product	Algorithm	ε_r (%)	RMSE $_{SPM \leq 10}$ (mg.l^{-1})	RMSE $_{SPM > 10}$ (mg.l^{-1})	R^2 (%)	N
MEGS8.1	TSM1 (Rrs_{665})	41.8	2.86	6.69	76.5	42
MEGS8.1	TSM2 (Rrs_{665} & Rrs_{620})	46.8	2.83	5.84	80.8	43
MEGS8.1	TSM3 (Rrs_{665})	40.1	1.61	7.71	73.7	42
MEGS8.1	Standard (NN)	40.0	2.56	6.45	79.4	46
SAABIO	TSM1 (Rrs_{665})	47.9	3.37	9.18	62.6	42
SAABIO	TSM2 (Rrs_{665} & Rrs_{620})	53.1	3.39	8.68	65.8	43
SAABIO	TSM3 (Rrs_{665})	37.0	2.02	6.52	79.3	42

A step-by-step statistical method (Fig. 2) was applied to raw SPM concentrations maps in order to discard images with too many flagged pixels on Rhône River turbid plume as follows:

1. Over all available images, a statistical analysis of SPM concentration was performed on the area of interest to determine a SPM threshold in order to identify the turbid plume from the background SPM concentration. For all images, SPM concentration distribution was analysed and the percentile 95 (the p^{th} percentile value is such that p % of the data are less than this value and (100-p) % are higher), *i.e.* 3 mg.l^{-1}, was chosen to be representative of the presence of the turbid plume.
2. Considering this threshold, a region of plume presence (ROPP) was identified using all available images, corresponding to pixels where at least 5 % of the SPM concentrations were above 3 mg.l^{-1}. This threshold is discussed later in section 4.
3. SPM concentration images with less than 80 % of valid pixels on the ROPP were discarded from the dataset.
4. A gap-filling method (Garcia, 2010), based on the discrete cosine transform and which has already proven its ability to deal with geophysical data analysis (Wang et al., 2012) was applied on the remaining images to build cloud-compensated images.

Finally, the dataset used for the present study is composed of the MERIS-300m acceptable data available on the area, *i.e.* 806 daily images from August 14th 2002 to April 7th 2012, then covering about 23 % of this period.

2.2 Turbid plume metrics extraction and data analysis

The Rhône River turbid plume is characterized by high SPM concentrations near the river mouth, decreasing with the cross-shore distance due to mixing, dilution and particle settling. Considering the shallow waters of the prodelta area and its waves exposure, deposited particles can be resuspended. As ocean color analysis does not permit yet to distinguish if SPM is either resuspended or directly coming from the river, we decided to remove all data where water depths are below 20 m, that we assume to be potentially impacted by wave-induced resuspension.

In order to delineate the turbid plume from clearer waters, the threshold denoting the presence of the turbid plume (3 mg.l^{-1}) was applied to the dataset. A routine was developed to

identify the turbid plume boundary and extract different metrics information: the area of extension (km^2); the southernmost, westernmost and easternmost positions, the centroid location and the schematic shape, called 'skeleton' in the present paper. Mean and maximum near-surface SPM concentrations within the turbid plume were also computed to provide information on seasonal and inter-annual variability of the turbid plume. Seasonal and inter-annual SPM spatial distributions were calculated considering the average of identified plumes.

In order to extract the area of extension of the Rhône River turbid plume, the number of pixels within its boundary was summed and converted to area unit (in km^2). Southernmost, westernmost and easternmost points were isolated directly from the boundary and the centroid corresponds to the average position of the pixels constituting the identified plume, regardless of their weight in terms of SPM concentration. The turbid plume schematic shape (skeleton) was computed considering the concentration gradient and the extreme points locations. The identified plume was divided in two parts: a proximal part (high SPM concentration), and a distal part (less concentrated). To identify each part, the same method aiming to isolate the turbid plume from clearer waters was applied inside the plume. The percentile 90 of the SPM concentrations of the plume was used as a threshold to separate distal and proximal parts, for each image. Centroids for both parts were computed and the turbid plume's skeleton was constructed joining (1) the Rhône River mouth, (2) the proximal plume's centroid, (3) the distal plume's centroid, and (4) one of the extreme points (southernmost, westernmost and/or easternmost), depending on the plume shape. If the plume is stretched out seaward, southernmost point is selected. If not, either the westernmost or the easternmost point is selected, depending in which direction it stretches out the most; and if the plume spreads out almost equally to the East as to the West, both easternmost and westernmost points are considered. Turbid plume metrics are shown on Fig. 2f.

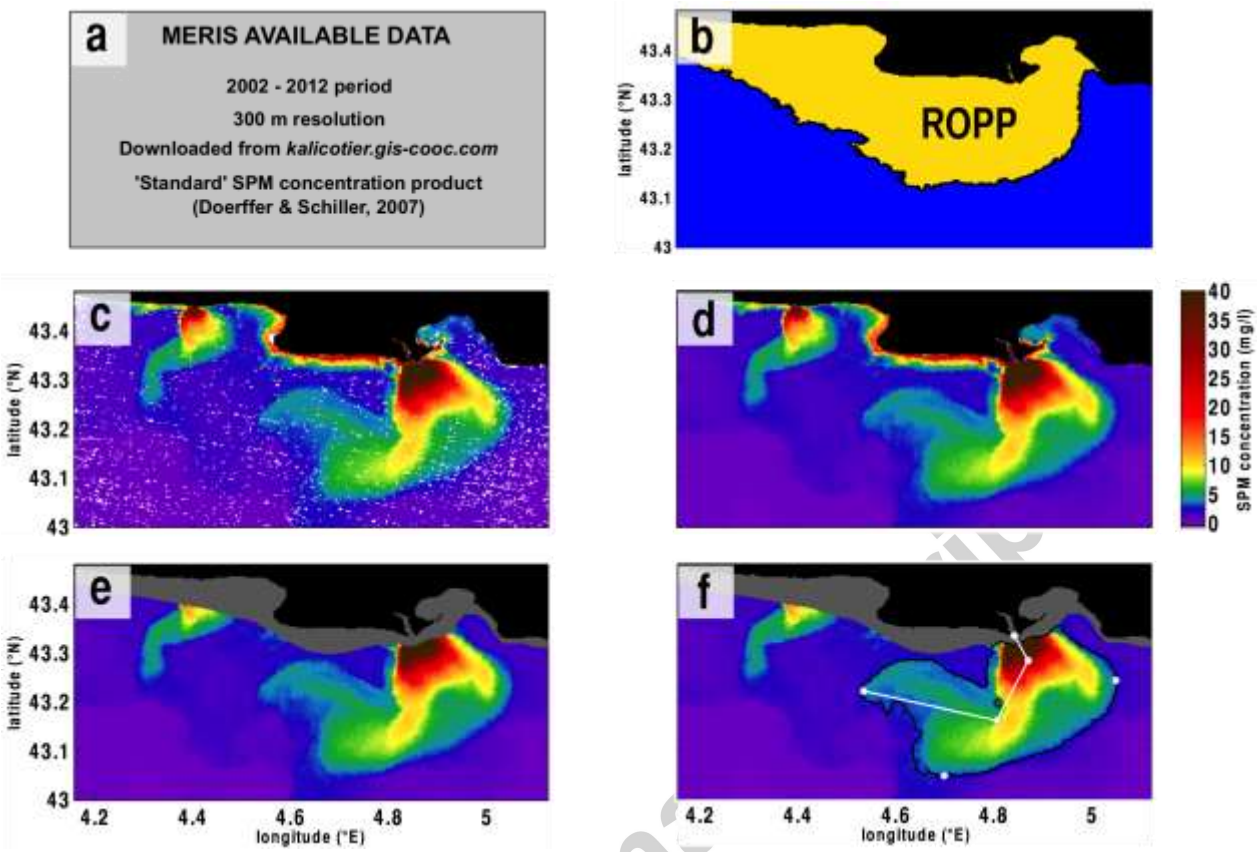

Figure 2: Summary of image selection and metrics extraction data processing: example of January 8th 2012. MERIS available data, summarized in (a), is used to determine the ROPP, which corresponds to the area where, for at least 5 % of all images, pixel value is over the SPM concentration threshold of 3 mg.l^{-1} (yellow domain in –b). For selected images (where at least 80 % of the data is available on the ROPP) containing flagged pixels (white ones in -c), a gap-filling method is applied (d). To avoid wave-induced resuspension and thus better identify the Grand Rhône turbid plume, pixels where water depths are below 20 m are flagged (grey ones in -e). Metrics are finally estimated considering a SPM concentration threshold of 3 mg.l^{-1}. (f): Plume centroid is represented here by a black dot, plume extension by the solid black line (area = 655 km^2), southernmost, westernmost and easternmost points are the white dots on the turbid plume's boundary, proximal and distal centroids are represented by the white dots inside the boundary. The skeleton is represented by the white line.

To highlight Rhône River turbid plume patterns, relationships between plume metrics and meteorological/hydrological forcings were investigated. We chose to study the plume response to the Rhône River water discharge (Q_w, in m^3.s^{-1}), the wind velocity (in m.s^{-1}) and wind direction (in degrees). The Rhône River discharge data were obtained from the French freshwater office database (http://www.hydro.eaufrance.fr), covering the study time period with daily measurements at the Beaucaire station (58 km upstream the Grand Rhône mouth). Wind velocity and direction at 10 m above sea level were extracted from three meteorological models provided by Météo-France to cover the entire study time period: the ALADIN model for the 19/06/2002 - 20/03/2006 period, the ARPEGE model for the 20/03/2006 - 24/11/2011 period, and the ARPEGE-HR model for the 24/11/2011 - 08/04/2012 period. Each image was associated with a river discharge value, a wind velocity and a wind direction. To consider turbid plume response time to these forcings, water outflow was averaged over the three days before satellite data

acquisition. Concerning the wind, pioneer work made by Demarcq and Wald (1984) indicated that the plume response time to wind forcing generally varied between few hours to 12 h and can be exceptionally higher, above 24 h for high water discharge values (Q_w > 4000 $m^3.s^{-1}$). Thus, we chose to associate each image to a wind (direction and intensity) averaged over 12 h before satellite acquisition.

Cloud-covered images were discarded from the dataset and MERIS-300m data does not provide daily acquisitions. Therefore the representativeness of the final dataset was investigated: the Rhône River water discharge (Fig. 3a) and wind conditions (Fig. 3b) over 2002-2012 were compared with the conditions associated to each image. Results showed a good agreement of water discharge ranges with a slightly overrepresentation of dry conditions (+ 5 % for Q_w < 1500 $m^3.s^{-1}$), balanced by an underrepresentation of higher discharge values (- 5 % for Q_w > 1500 $m^3.s^{-1}$). Considering winds, southern and eastern winds are underrepresented, and it is especially the case for strong SE winds (> 10 $m.s^{-1}$). These onshore winds, mainly blowing during the winter period, are known to bring clouds over the study area, which explains the underrepresentation highlighted by the analysis. Fig. 3b clearly identifies two main wind sectors, characteristic of the study area: north-western to northern ones (295° to 15°) and south-eastern ones (80° to 160°), qualified hereafter as "onshore winds". We therefore chose to consider these two sectors to study relationships between plume metrics and meteorological forcings.

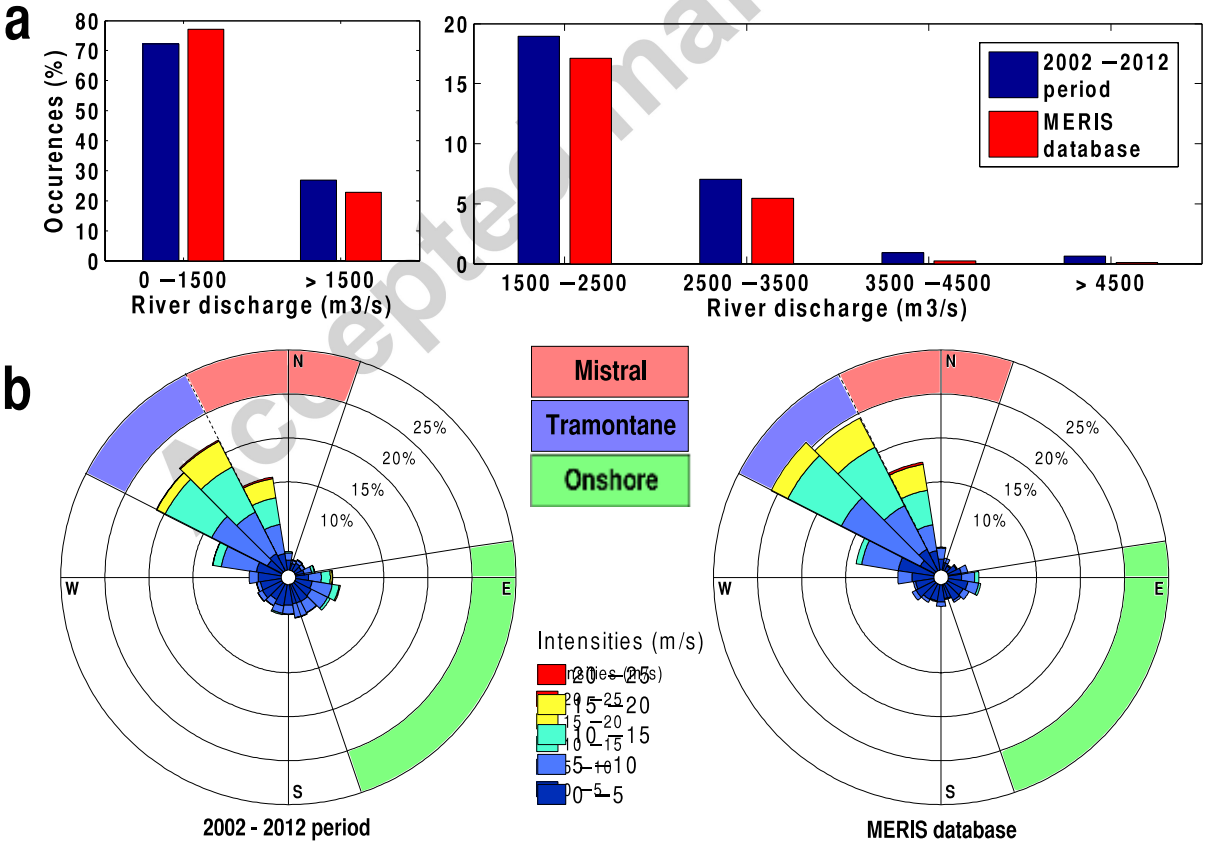

Figure 3: Meteorological conditions representativeness of the MERIS dataset used in this study for (a) Grand Rhône River discharges (occurrences in %) and (b) averaged wind directions and intensities over 2002-2012 (left part – daily average)

and for the MERIS dataset (right part – daily average). Blue bars in (a) represent typical outflow conditions and red bars the conditions associated to the post-processed MERIS data.

3 Results

3.1 Seasonal and interannual variability of the Rhône River turbid plume

The Rhône River turbid plume dynamics is studied through monthly averaged near-surface SPM concentration maps over the 2002-2012 period (Fig. 4) and the analysis of metrics statistics such as plume area and its maximum and mean SPM concentrations (C_{mean} and C_{max}, respectively - Fig. 5).

Results presented in Fig. 4 show that during November, December and January, the Rhône River turbid plume is the largest and the most concentrated, with averaged concentrations always higher than 15 mg.l^{-1} near the river mouth (for water depth higher than 20 m) and up to 5 mg.l^{-1} 10 km offshore. Statistics in Fig. 5 show that, during this period of the year, for 25 % of the time, the plume expands over 250 km^2 (over 320 km^2 for December and January) and C_{mean} and C_{max} reach values from 7 to 8 mg.l^{-1} and 33 to 44 mg.l^{-1}, respectively. From February to April, the turbid plume covers a smaller area (with median values always below 50 km^2) and is less turbid than for the three previous months as averaged concentrations never exceed 14 mg.l^{-1} near the river mouth (maximum recorded in February). For 25 % of the time, the turbid plume expands on 130 to 160 km^2, with C_{mean} and C_{max} values ranging from 5 to 6 mg.l^{-1} and 21 to 24 mg.l^{-1}, respectively. From May to October, a small (median area ranging from 5 to 32 km^2) and diluted plume is observed, featured by low average concentrations: C_{mean} and C_{max} median values range from 4 to 5 mg.l^{-1} and 6 to 10 mg.l^{-1}, respectively. This seasonal trend of the turbid plume area, C_{mean} and C_{max} is also observed for the Grand Rhône River discharge. Fig. 5 also shows an interannual variability for the turbid plume area, C_{mean} and C_{max}, which is the strongest for the months where the turbid plume is the largest. This variability can be explained by the variability of the Rhône River discharge and related sediment input, following exactly the same trend. During the summer/autumn period, June is atypical as metrics show unexpected high variability: values of first and third quartiles range from 4 to 200 km^2 and 4.5 to 17 mg.l^{-1} in terms of area and maximum concentration, respectively. This month is particularly interesting because of its dispersion and that the median value for all these metrics is similar to the one of the month of February for instance, where larger and more concentrated plumes are expected. This dispersion is explained by the strong inter-annual variability of the Rhône River turbid plume metrics, shown on Fig. 6 and Fig. 7. A year-by-year statistical analysis highlights that the years 2007-2008-2010, where large and concentrated plumes were observed, correspond to wet years, with median river discharges higher than 1600 m^3.s^{-1}.

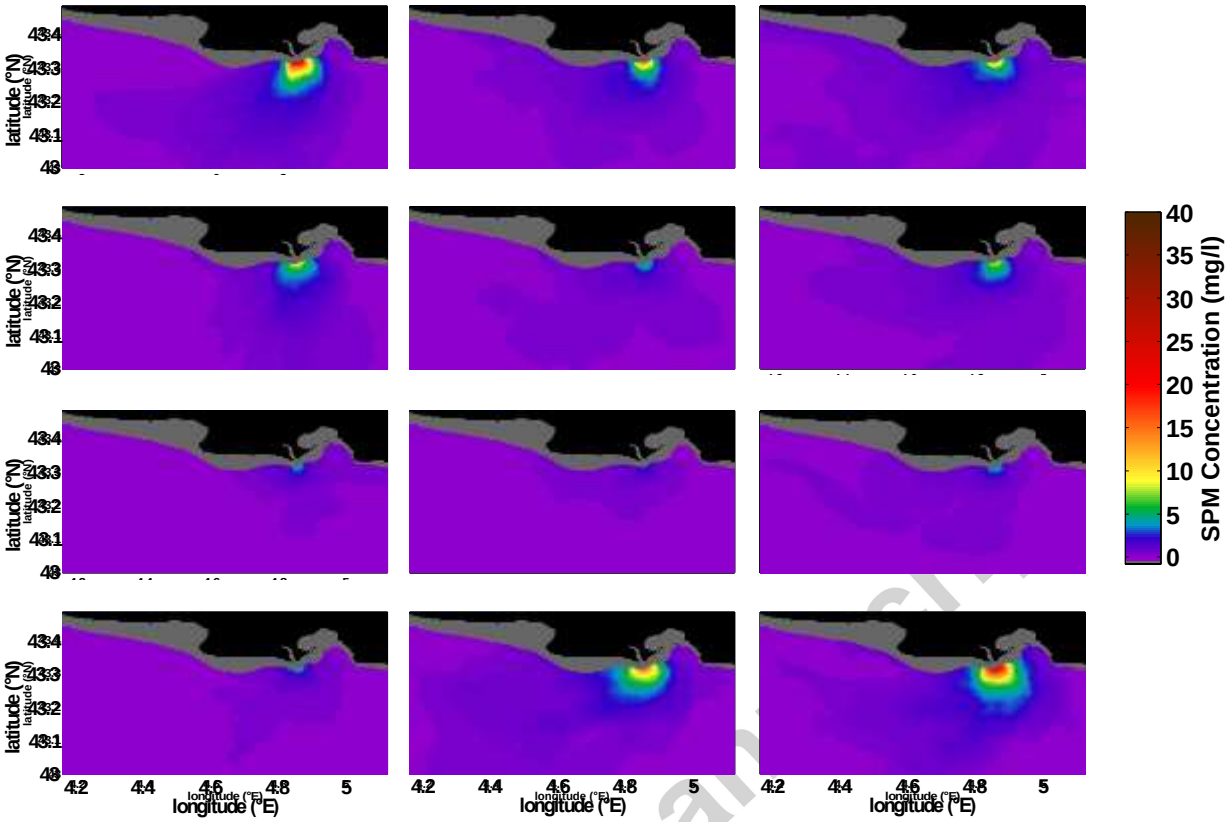

Figure 4: Monthly averaged plume SPM concentration maps over the 2002-2012 period. SPM concentrations values corresponding to water depths lower than 20 m are flagged (grey color). *m* and *n* are months and the number of images used for the averaging, respectively.

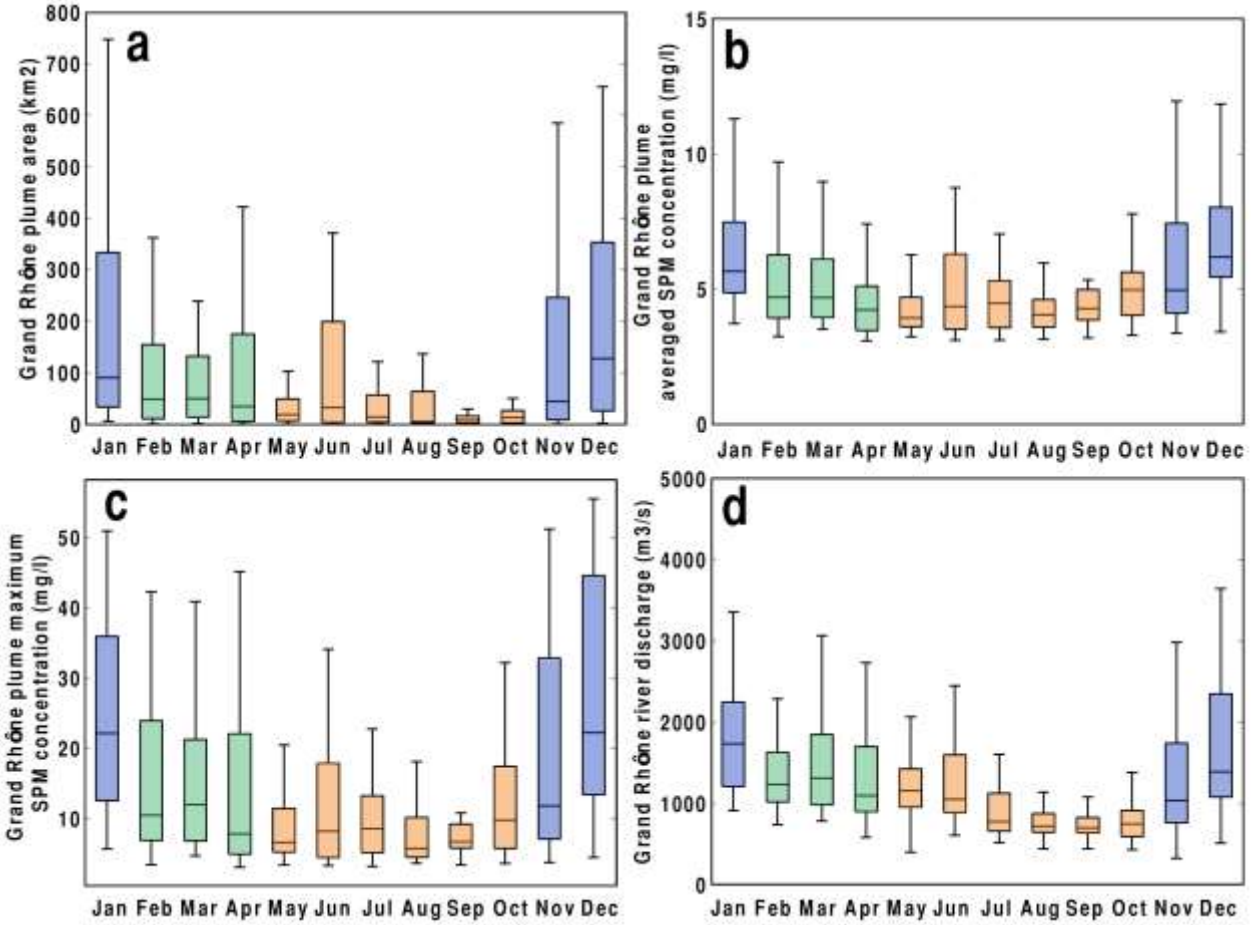

Figure 5: Monthly averaged data and products considering water depths higher than 20 m for Grand Rhône River plume (a) extension (km^2), (b) averaged SPM concentration ($mg.l^{-1}$) and (c) maximum SPM concentration ($mg.l^{-1}$) calculated over the 2002-2012 period. Outflow variability over this period is presented in (d). Colors represent the three different seasons identified. Line inside each box: median; lower and upper whiskers: minimum and maximum values not considering the outliers*, respectively; lower and upper box limits: first and third quartiles, respectively.

***outliers are definied to be greater than $q_3 + w \times (q_3 - q_1)$ or less than $q_1 - w \times (q_3 - q_1)$, where q_1 and q_3 are first and third quartiles, respectively, and w is the whisker value.**

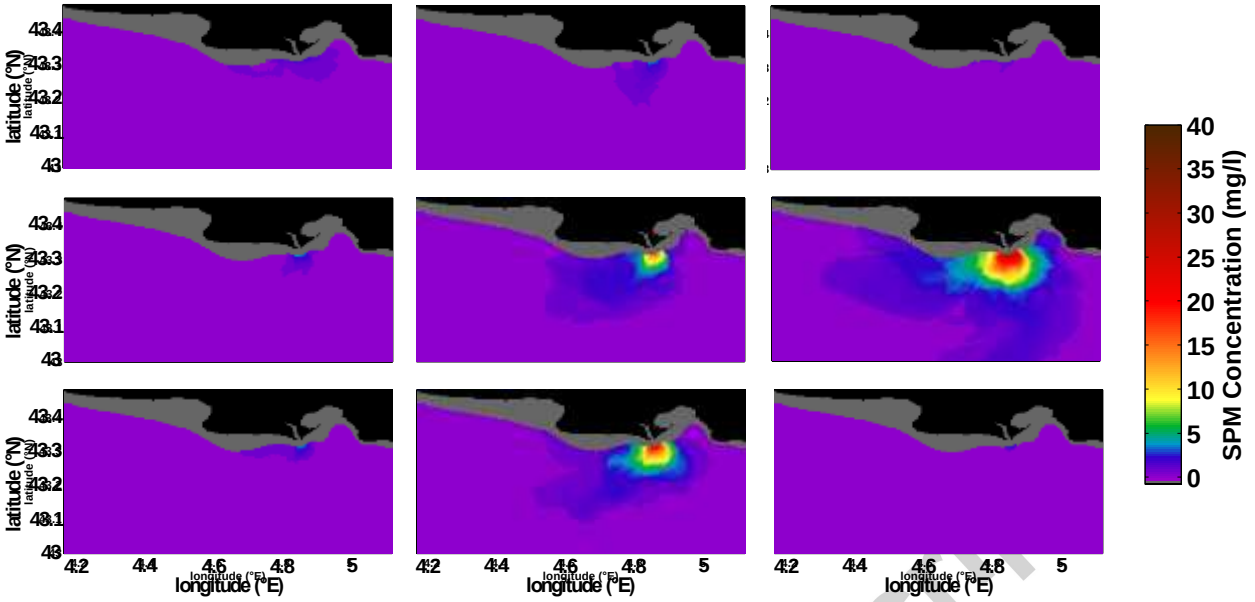

Figure 6: Interannual variability of Rhône River turbid plume for the month of June. SPM concentrations values corresponding to water depths lower than 20 m are flagged (grey color). *y* and *n* are years and number of images used for the avearging, respectively.

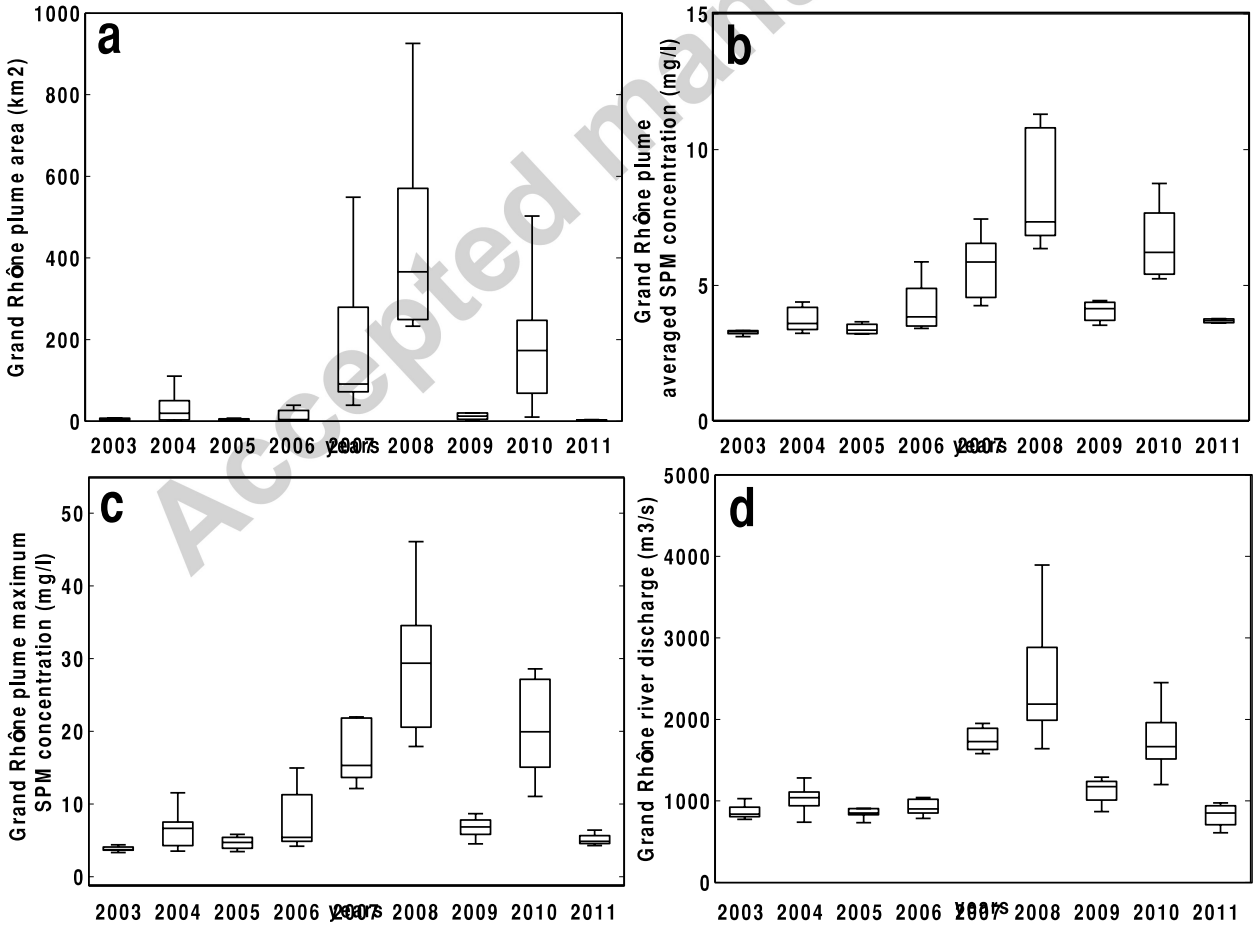

Figure 7: Metrics yearly statistics for the month of June considering water depths higher than 20 m for Grand Rhône plume (a) extension (km^2), (b) averaged SPM concentration ($mg.l^{-1}$) and (c) maximum SPM concentration ($mg.l^{-1}$) calculated over the 2002-2012 period. Outflow variability over this period is presented in (d). Lines inside each box: median; lower and upper whiskers: minimum and maximum values not considering the outliers*, respectively; lower and upper box limits: first and third quartiles, respectively.

***outliers are definied to be greater than $q_3 + w \times (q_3 - q_1)$ or less than $q_1 - w \times (q_3 - q_1)$, where q_1 and q_3 are first and third quartiles, respectively, and w is the whisker value.**

3.2 Turbid plume dynamics: response to hydro-meteorological forcings

As monthly average results showed strong variability, it is interesting to use daily (when available) information of the Rhône River turbid plume metrics to investigate its high frequency variability and to link it to the hydro-meteorological forcings. To this end, the turbid plume metrics were separated in two groups, depending on the prevailing winds direction: offshore winds (Mistral and Tramontane - 335° to 15°) and onshore winds (80° to 160°). These two groups represent 71 % of the database.

The positive trend observed at the seasonal scale between water discharge (3 days average) and turbid plume area is confirmed by the high frequency analysis (Fig. 8a). For outflows higher than 1500 $m^3.s^{-1}$, the turbid plume expands on a surface always larger than 10 km^2, 20 % of the time larger than 100 km^2 and can reach values up to more than 1000 km^2. For dry conditions (Q_w < 1500 $m^3.s^{-1}$), the turbid plume is often small (44 % under 10 km^2 and 92 % under 100 km^2) but can expand very episodically up to 550 km^2 for onshore winds. This same positive trend can be observed on Fig. 9a, linking the circles size (representing plume area) to the colour scale (representing the Grand Rhône River discharge), for offshore winds conditions. For dry conditions (Q_w < 1500 $m^3.s^{-1}$), the turbid plume's centroid is located for 95 % of the time at less than 7 km seaward from the Grand Rhône River mouth (43.2662° N latitude). However, for water discharges higher than 1500 $m^3.s^{-1}$, the centroid is for 64 % of the time located at more than 7 km seaward.

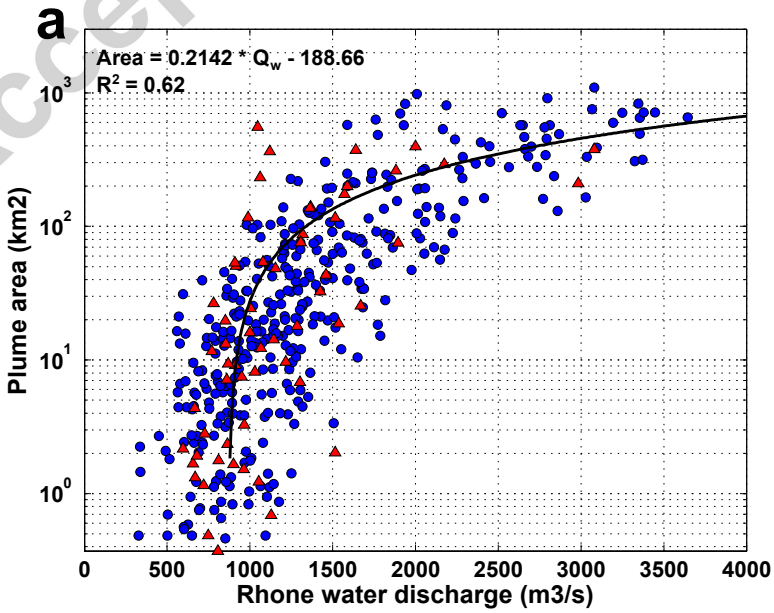

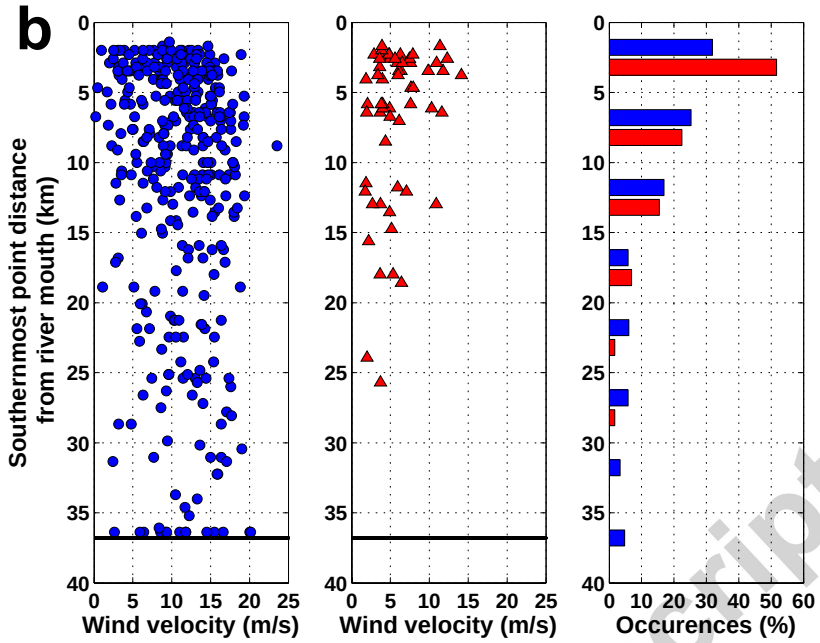

Figure 8: Rhône River turbid plume response to (a) water discharge and (b) prevailing winds. Blue and red colours are associated to Mistral + Tramontane winds (295° to 15°) and onshore winds (80° to 160°), respectively. The solid black line in (b) represents the southern boarder of the study area.

Concerning meteorological forcing, Fig. 8a shows that wind orientation does not impact the global relationship linking water discharge and turbid plume area. However, it is noticeable that for high river discharges (Q_w > 2000 $m^3.s^{-1}$) and onshore wind conditions, the Rhône turbid plume does not expand as much as it is the case during offshore wind conditions. Indeed, for onshore winds, the area ranges from 200 km^2 to 400 km^2 (with a mean value of ~ 290 km^2), whereas in offshore wind conditions, areas range from about 100 km^2 to more than 1000 km^2 (with a mean value of ~ 400 km^2).

Fig. 8b highlights that onshore winds (in red) tend to confine the turbid plume along the coast as in these conditions, it never expands further than 26 km offshore (74 % below 10 km) whereas Mistral and Tramontane winds stretch the plume seaward up to the limits of the study area. Wind velocity does not seem to affect directly the southern extension of the turbid plume during offshore wind conditions, unlike for onshore wind ones: the stronger the wind is, the more alongshore the plume is.

Fig. 9a also shows the confining of the turbid plume during onshore wind conditions as centroids are clearly located northern of the study area compared to Mistral and Tramontane winds. The mean offshore distance of plume centroid for various ranges of water discharges, reported on Table 2, confirms this observation. The skeleton representation of the turbid plume (Fig. 9b) also indicates that, for onshore winds, the Grand Rhône River turbid plume is located at the north of the study area, with almost isotropic orientations. For Mistral and Tramontane winds, the higher the discharge rate, the more defined the turbid plume is. Indeed, for low river discharges (Q_w < 1500 $m^3.s^{-1}$), the plume orientation is almost isotropic whereas for higher

discharge rates ($Q_w \geq 1500$ $m^3.s^{-1}$), the orientation is better defined, showing a southwestward to westward deflection of the distal part of the plume, giving to the turbid plume a "coma shape".

Table 2: Mean area (km^2) and centroid offshore distance (km) of the Grand Rhône River turbid plume.

	Mistral and Tramontane winds		Onshore winds	
	mean area (km^2)	mean offshore distance of the centroid (km)	mean area (km^2)	mean offshore distance of the centroid (km)
$Q_w < 1500$ $m^3.s^{-1}$	28.6	3.4	48.4	2.9
$1500 \leq Q_w < 3000$ $m^3.s^{-1}$	234.4	9.5	178.2	4.9
$Q_w \geq 3000$ $m^3.s^{-1}$	649.0	15.5	376.3	3.5

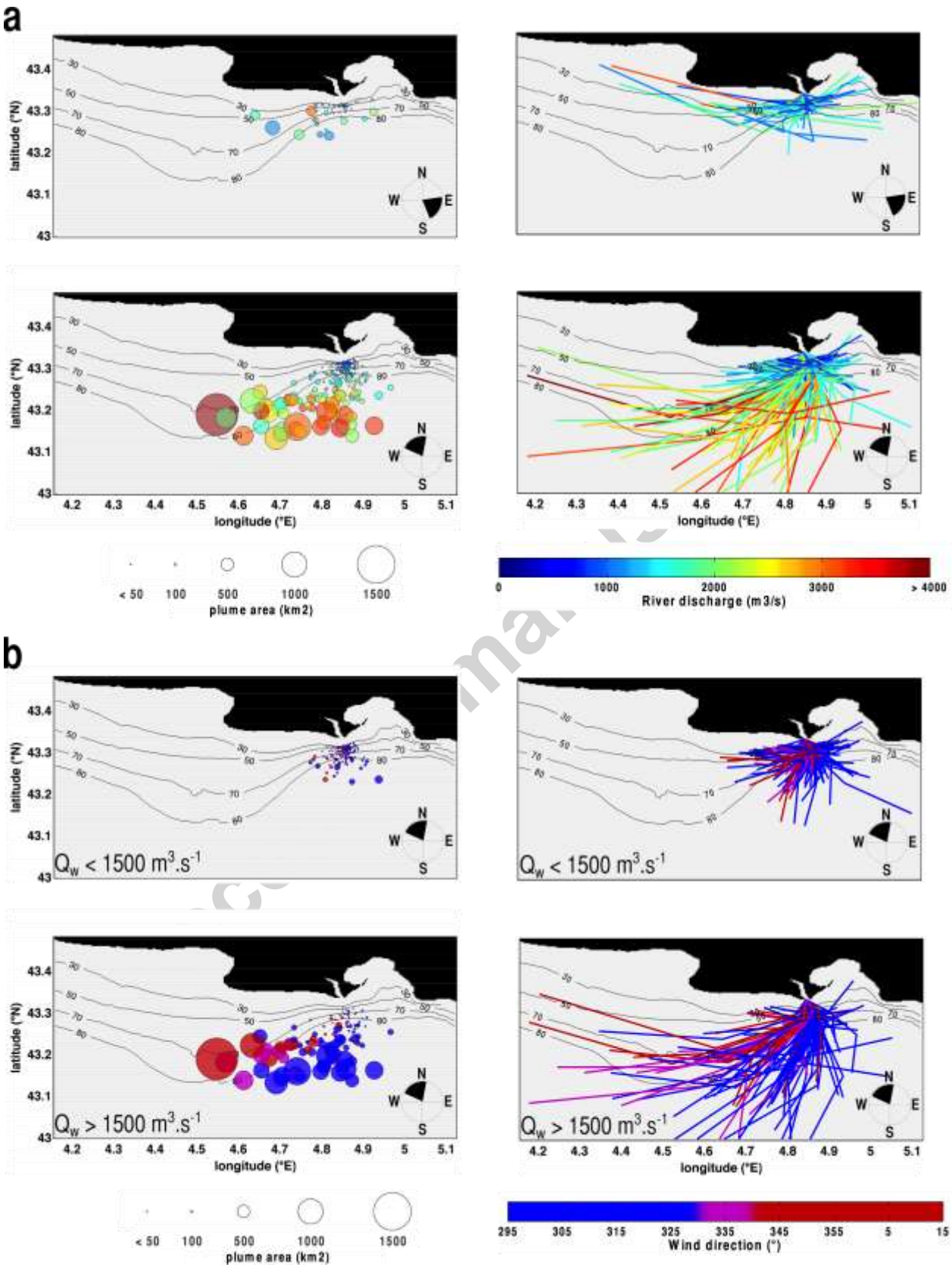
a
b
latitude (°N)
longitude (°E)
43.4
43.3
43.2
43.1
43
4.2
4.3
4.4
4.5
4.6
4.7
4.8
4.9
5
5.1
N
W
E
S
Q_w < 1500 m^3.s^{-1}
Q_w > 1500 m^3.s^{-1}
< 50
100
500
1000
1500
plume area (km2)
0
1000
2000
3000
> 4000
River discharge (m3/s)
295
305
315
325
335
345
355
5
15
Wind direction (°)

Figure 9: Rhône River turbid plume's centroids (circles) and skeletons (solid coloured lines) for Mistral, Tramontane (NW to N) and Onshore winds (E to SE). The more extended is the plume, the bigger is the circle representing its centroid. Colour is associated to (a) river discharge ($m^3.s^{-1}$) or (b) northern winds direction (degrees). For each illustration, a wind rose reminds the wind orientation associated. In (b), dry conditions (Q_w < 1500 $m^3.s^{-1}$) are separated from wet ones (Q_w > 1500 $m^3.s^{-1}$) for more visibility (indicated on illustrations). Smallest points (areas < 100 km^2) are blue to dark blue.

A positive linear relationship was also derived for mean and maximum concentrations detected by the satellite as a function of the Rhône River discharge (Fig 10). As an example, maximum concentrations range from 5 $mg.l^{-1}$ to 35 $mg.l^{-1}$ for average discharge conditions while they reach 35 $mg.l^{-1}$ to 50 $mg.l^{-1}$ for river discharges larger than 3000 $m^3.s^{-1}$. Given the correlation coefficients, the river discharge explains 54 % and 72 % of Rhône River plume C_{mean} and C_{max}, respectively. Similarly to the turbid plume area dynamics, wind orientation does not dominantly drive the SPM concentration variations, as offshore/onshore scatters are not associated with two distinct populations. However, it is remarkable that mean and maximum concentrations during onshore wind events are significantly lower than during offshore events, and especially for low to moderate river discharges (lower than the mean river discharge). Nevertheless, these differences should be considered with attention as they could be caused by the exclusion of the very close coastal domain (*i.e.* where depth are lower than 20 m), where the plume could main develop in case of strong onshore winds. These differences are discussed in section 4.

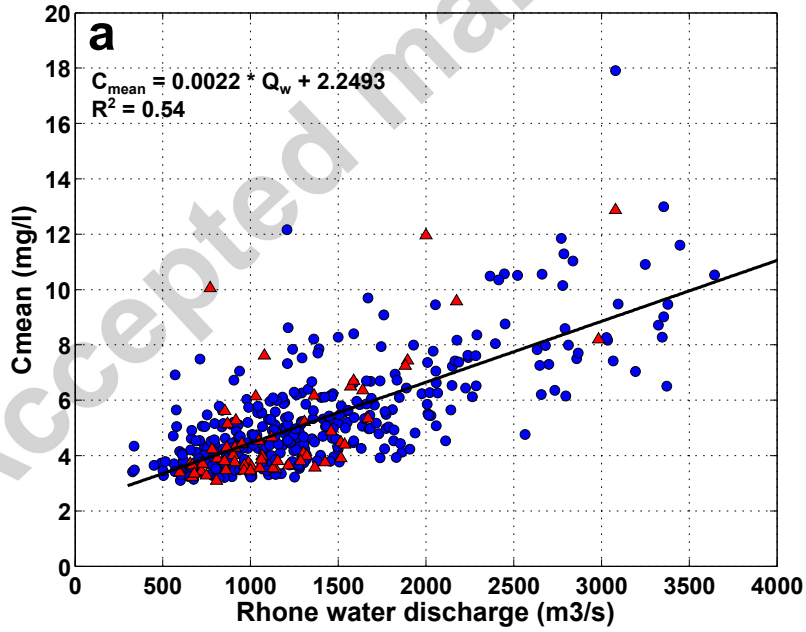

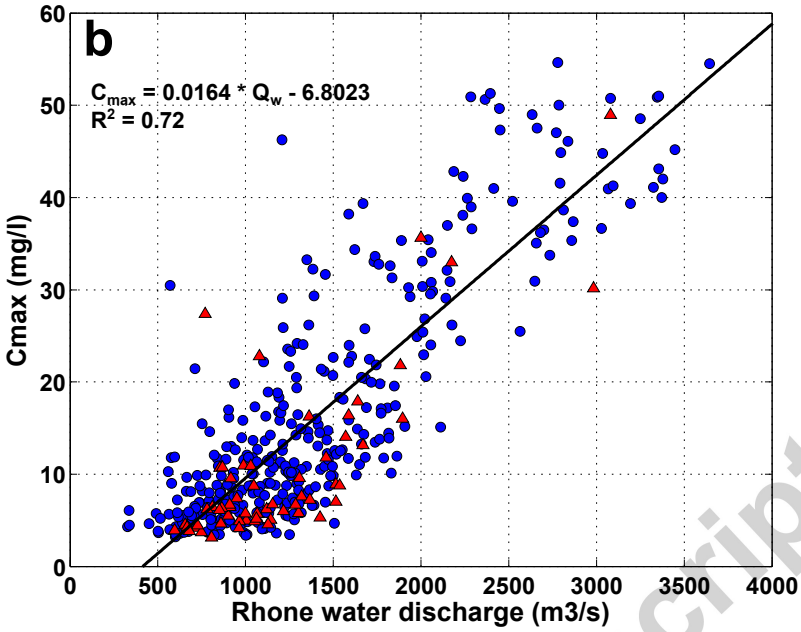

Figure 10: Correlations between Rhône River discharge and turbid plume (a) mean SPM concentration (C_{mean}) and (b) maximum SPM concentration (C_{max}).

4 Discussion

4.1 Database constitution

Flood conditions are responsible for 80 % of the total Rhône River particulate inputs in the GoL (Roditis and Pont, 1993; Rolland, 2006) and their impact is thus of critical importance in the study of sediment dynamics. However, it is difficult to collect valuable satellite data during these events as they are often related to important rainfall, and thus cloudy weather conditions. The 806 images constituting the MERIS-300m dataset in this area cover 23 % of the 08/14/2002 to 04/07/2012 period and the missing information is almost equally divided between dry ($Q_w \leq$ 1500 $m^3.s^{-1}$) and other ($Q_w >$ 1500 $m^3.s^{-1}$) conditions, as shown in the left illustration of Fig. 3a. Nevertheless, the study of the dataset representativeness also reveals that, for high river discharges (*e.g.* $Q_w \geq$ 2500 $m^3.s^{-1}$), the higher is the discharge, the less it is represented in the dataset: 22 %, 73 % and 81 % of 2500 < $Q_w \leq$ 3500 $m^3.s^{-1}$, 3500 < $Q_w \leq$ 4500 $m^3.s^{-1}$ and $Q_w >$ 4500 $m^3.s^{-1}$ events are missing, respectively (right part of Fig. 3a). Concerning wind conditions, the MERIS database is shown to underrepresent meteorological conditions associated to onshore winds (Fig. 3b), with 46 % of missing values for winds of velocity higher than 4 $m.s^{-1}$ (representing 13% of the events from the full dataset and only 7% in the MERIS database used for analysis). This underrepresentation is explained by the advection of clouds over the study area by these winds. Despite these missing data, the database is sufficient to provide a good overview of the Rhône River turbid plume and explore its response to different hydro-meteorological conditions.

4.2 Threshold for plume detection

Choosing a concentration threshold for detecting turbid plume from ambient background concentration is highly challenging. Field measurements show that marine, offshore GoL concentrations range from 0.7 to 2.2 $mgl.l^{-1}$. We chose, in this study, to derive the threshold from a statistical analysis of near surface SPM concentration maps. We first assumed that, in the Gulf of Lions, the presence of high turbidity at the surface is exceptional, and located either close to the coast and in the neighboorhood of river mouths. Next, for embedded areas centered on the rhone river mouth (Fig. 11a), we estimated the percentile 95 of the SPM concentrations observed by the satellite in each area and for all images available. We observed that this value follows a plateau around 3 $mg.l^{-1}$ for areas larger than 5000 km^2, and suddenly increased towards the smallest areas (*i.e.* below 5000 km^2), close to the rhone mouth (Fig. 11b). Hence we considered that this plateau corresponds to the ambient background concentration observed by the satellite in the GoL. We also tested the sensitivity of our analysis to this thereshold, and compared the detected areas for threshold values of 3 $mg.l^{-1}$ and 4 $mg.l^{-1}$ (Fig. 12). As expected, a larger threshold results in the detection of smaller plume areas (approximately 23 % lower) but this shift follows a linear trend, and hence does not impact the global analysis and the correlation or relationship between metrics and forcings.

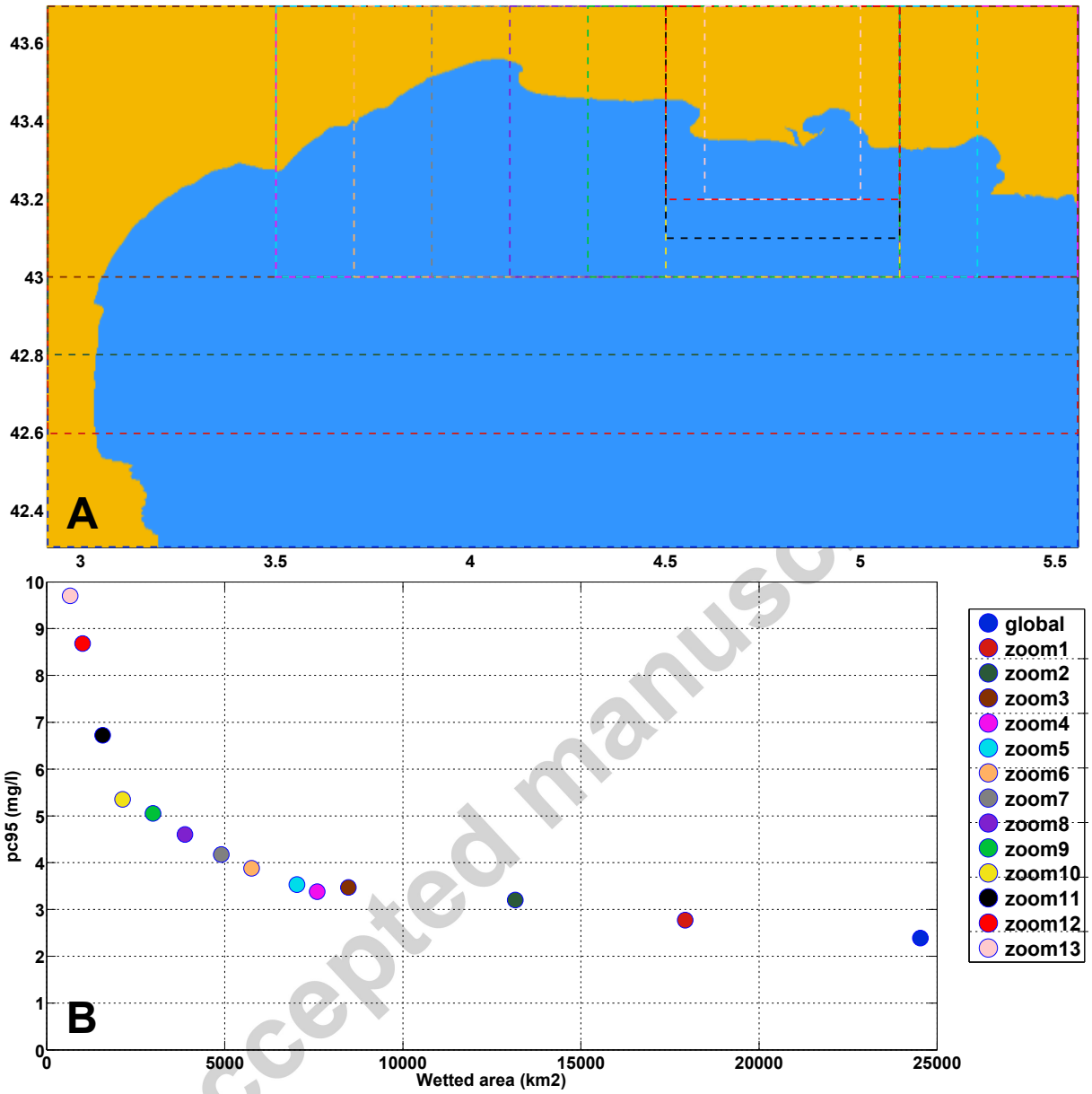

Figure 11: (a) embedded areas tested for the statistical analysis leading to the choice of the threshold value for turbid plume extraction and (b) associated pc95 values of SPM concentration (mg.l^{-1}) regarding each area. Scatters color corresponds to the color of embedded areas.

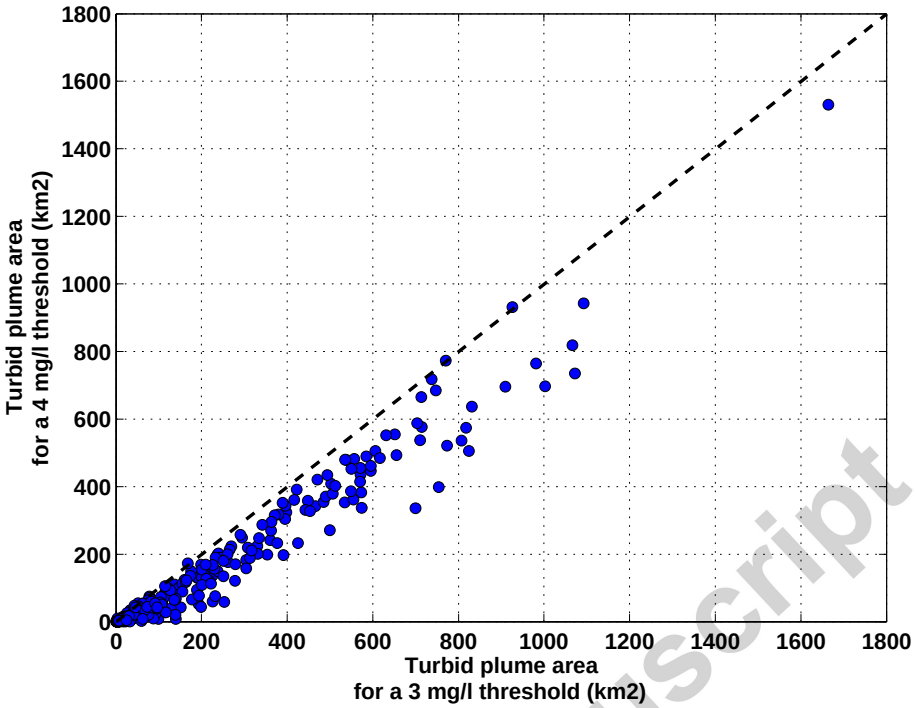

Figure 12: Sensitivity of turbid plume area extraction to threshold selection for values of 3 mg.l^{-1} and 4 mg.l^{-1}.

The same threshold value of 3 mg.l^{-1} was used by Petus et al. (2014) in the study of the Adour River turbid plume metrics, determined from field data collected in 2007 (Petus et al., 2010). In a second step, pixels where water depth is below 20 m were discarded from the analysis. This mask was applied because for these water depths, numerical modelling showed that bottom shear stress (BSS) values are higher than 0.2 N.m^{-2} for at least 10 % of the time (Dufois et al., 2008). This value is close to the critical shear stress of 0.35 N.m^{-2} used in the simulations of Dufois et al. (2014) for muddy sediments. Therefore, bottom resuspension in shallow areas can be significant as well as their contribution to the surface turbidity signal. This could bias the surface plume detection, which justifies why a 20m-mask was applied to the ocean color data, and visually checked. This choice induces a systematic underestimation of the plume extension area, and for very dry conditions, the plume could potentially not be detected at all. Indeed, for Mistral and Tramontane wind conditions, an area of 15 km^2 in front of the Grand Rhône River mouth is not taken into account for the plume metrics calculation. This value is higher for onshore wind conditions as the flagged area is of about 230 km^2 (along the coast from Grand Rhône River mouth to Petit Rhône River mouth). A sensitivity study to the bathymetric flag (20 m) was performed over onshore-winds associated SPM concentration maps. Results (Fig. 13) revealed that values are biased (but with a mean bias of 46 km^2) and significantly impact metrics for plume covering areas smaller than 50 km^2 (underestimating plume area from 20 % to 100 % for the smallest plume area). These differences in metrics are observed both in presence of low wind, *i.e.* without waves, or high wind, *i.e.* potentially with waves resuspending bottom sediments, up to the sea surface (Dufois et al., 2014). In the same way, mean and maximum SPM concentrations for onshore wind conditions can be underestimated of about 1 mg.l^{-1} and 5 mg.l^{-1},

respectively. Taking this bias into account would bring these values closer to the offshore wind associated values and of regression lines of Fig. 10.

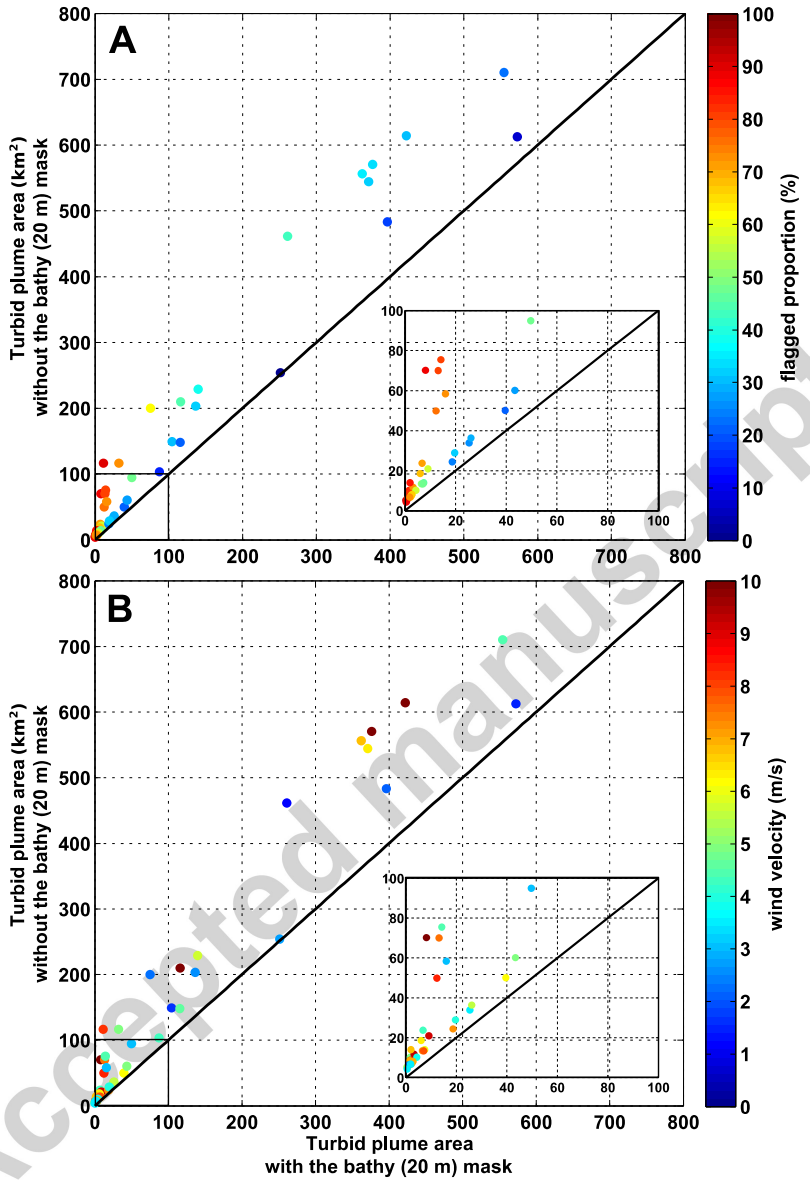

Figure 13: Turbid plume area underestimation for onshore winds conditions. Color scale shows (a) flagged area proportion (%) and (b) wind velocity (m.s^{-1}). The solid black line represents the 1:1 line. Embedded graphs show a zoom over the 0-100 km^2 range.

4.3 Turbid plume response to hydro-meteorological forcings

The day-by-day analysis confirms the positive correlation between the Rhône River water discharge and the extension of the turbid plume area. The dispersal scaling relation proposed by Warrick and Fong (2004) ($P = cA^b$ where P is plume area, A the watershed area and b and c regionally-based constants) was tested on our dataset on the Rhone river plume. Considering a decennial flood value of the Rhône River (about 7600 m^3.s^{-1}), the estimated plume area for the

relationship described in this paper led to a 0.63 coefficient, in the range of values (0.68 +/- 0.04) found by Warrick and Fong (2004) in their study comparing different rivers of the world for "special events". Onshore and offshore wind-generated plumes behave the same in response to the river outflow (red triangles are predominantly grouped with blue circles on Fig. 8a). The three red triangles isolated from the point cloud (Q_w ~ 1100 $m^3.s^{-1}$ and area greater than 200 km^2) correspond to one particular event (February, the 12th, 13th and 15th 2008) and not to three different periods. This event can also explain why the averaged area for Q_w < 1500 $m^3.s^{-1}$ and onshore wind conditions seems high compared to its corresponding value for offshore wind conditions (Table 2). Indeed, discarding these three days from the average calculation, the averaged area would drop down to 25 km^2. Considering the systematic under-estimation of turbid plume area by the wave mask, plume areas associated to onshore winds would be proportionally more underestimated as they are more often located along the coast (Fig. 9a). From Fig. 8a, it is noticeable that, even if the two populations follow the same trend, onshore wind associated plume areas rise to a level much below the one for Mistral and Tramontane associated ones. For onshore wind conditions, the turbid plume can expand up to 400 km^2 (with a potential maximum underestimation of about 200 km^2 due to wave-mask) while, for offshore wind conditions, it can expand up to more than 1000 km^2. It is also visible on the centroid representation of Fig. 9a, where the biggest circles, corresponding to the largest plumes, are smaller for onshore winds conditions than for Mistral and Tramontane ones.

N/NW winds strongly drive the surface circulation towards the south, which explains why the plume extends southern during these conditions. On the contrary, onshore wind drive the surface circulation Northward, and explain the location of the plume close to the coast. For Mistral and Tramontane wind conditions, when turbid plumes are stretched to the south, they are globally deflected to the west under the Coriolis effect and the influence of the Northern Current, flowing westward along the shelf slope. Fig. 9b highlights a different orientation of the plume either in the case of Mistral winds (N) or Tramontane ones (NW): first ones tend to promote a southwestward expansion and the latter a southward one. This is particularly visible during wet conditions (Q_w > 1500 $m^3.s^{-1}$), where turbid plume's centroids associated to northwestern winds are located at the west of northern winds associated ones. Skeletons, representative of the plume's shape, also confirm this observation. This observation agrees with the Ekman (1905) theory on the relationship between wind and surface currents and (Demarcq and Wald, 1984) observations, establishing that the Rhône River plume is deflected by about 50° on the right side of the wind.

4.4 Using metrics for comparing coastal system dynamics

Metrics are useful proxies for investigating large scale and dynamic coastal structures such as turbid plumes. They provide time series of key features such as plume area or centroid position, which can be confronted to forcings as in the present study to examine the short term to long term plume dynamics (*i.e.* in the future, the impact of global change). Metrics provide also valuable information when comparing observations and numerical model results: identical

parameters are then calculated from the different datasets and can be dynamically compared, complementary to raw day-by-day satellite data analysis. Finally these metrics can be used to compare the dynamics of different coastal systems, and evaluate and scale their sensitivity to driving forcings such as tide, wind, or discharge (suspended solids or water fluxes).

Studies on river plume dynamics using metrics are still scarce but data could be found for different systems. Here, we propose a comparison of plume metrics data for the Rhône River (present study), the Mississippi River (Walker, 1994), the Ebro River (Fernández-Nóvoa et al., 2015) and the Adour River (Petus et al., 2014). Primarily, it is appropriate to mention that each group of authors did use a different criterion to discriminate the turbid plume from the surrounding waters. For the Rhône River, it is described in the section 2.2 of this paper. Concerning the Mississippi River, Walker (1994) decided that the turbid plume is defined as areas where SPM concentration is above 10 $mg.l^{-1}$ but no further information was found on this choice. Petus et al. (2014)chose to delineate the turbid plume from the surrounding waters with a SPM concentration threshold of 3 $mg.l^{-1}$ on behalf of in situ measurements carried out during a field campaign (Petus et al., 2010). Fernández-Nóvoa et al. (2015) tested a large range of turbid threshold values and selected the one with the maximum Pearson correlation coefficient between plume area and river discharge, meaning that they assumed *a priori* that the plume area is linearly correlated to the river discharge.

Fig. 14 shows the superposition of the responses of the turbid plume area regarding the water and solid river discharges for the Rhône River, the Mississippi River, the Ebro River and the Adour River. The Ebro, the Rhone and the Adour systems are characterized by similar river forcing and turbid plumes can be ordered as follow: for a given discharge, Rhone plume areas are smaller than the Adour plumes, which are smaller than the Ebro plumes. The Mississippi system differs from the 3 others by river discharges about one order of magnitude larger than the three others, both in term of water discharge and solid discharge. However, the Mississippi plume dynamics ranges between the Rhone and the Adour dynamics once extrapolated to the Mississippi discharges (even if these extrapolations must be considered with care as they are not representative of the real dynamics of the Adour and Rhone systems).

Rhône River and Mississippi River

These systems have similarities: they are both wind-driven (Murray, 1972; Schroeder et al., 1987), subjected to a westward geostrophic flow (Schroeder et al., 1987) and to weak tidal currents in general, with an average tidal range of about 30 cm (Murray, 1972). However, the vorticity within the near Mississippi Delta region could be stronger, with the presence of two recirculation cells on both side of the delta (Cochrane and Kelly, 1986; Rouse and Coleman, 1976), which may explain why the Mississippi turbid plume area is larger than the Rhone turbid plume area once extrapolated to river discharges above 10000 $m^3.s^{-1}$.

Rhone River and Adour River

The relationship between the river discharge and the solid discharge for these two systems is significantly different, especially for river discharges lower than 1000 $m^3.s^{-1}$, when the Adour River delivers about one order of magnitude more suspended sediments to its delta than the Rhône River (Fig. 15). Hence sediment supply may explain the difference in plume patterns. Moreover, the Adour River turbid plume is significantly larger than the Rhone River turbid plume for similar solid discharges (Fig. 14b). These differences could be explained by the hydrodynamic regime of these two systems. Contrary to the Rhône River, the Adour estuary is a macro-tidal system with a tidal range varying between 2 m and 5 m (Stoichev et al., 2004). Petus et al. (2014) suggested that the tide affects the river plume area, and hence this forcing would contribute to disperse the plume on larger areas for similar river discharge.

Rhone River and Ebro River

Different plume patterns are observed for these two Mediterranean microtidal coastal systems: the Ebro plume signature is characterized by areas about one order of magnitude larger than the Rhone river plumes, for similar discharge values. However, the Ebro system is located close to the Rhone Delta, controlled by similar wind regimes (Mestres et al., 2003) and driven by the Northern Current, which is flowing with maximum speeds of several 10 $cm.s^{-1}$ about 40 km offshore the Rhône River mouth (Millot and Taupier-Letage, 2005) and from 0.1 to 0.5 $m.s^{-1}$, also about 40 km off the Ebro River mouth (Font et al., 1990). These similarities may discard the hydrodynamic regime to be responsible of these different patterns. Also the Ebro plume area is one order of magnitude larger than the Adour plume, while the Adour solid discharge is significantly larger than Ebro. We assume that the differences could be induced by the methodological approach applied to delineate the turbid plume boundaries.

Finally, variability in suspended sediment behaviour driven by flocculation processes (*i.e.* the settling velocity), may contribute to induce differences in turbid plume dynamics. Unfortunately no data related to suspended sediment (floc) dynamics are currently available on the investigated systems. However this parameter should be further studied for a global understanding of coastal dynamics.

The methodology applied to detect turbid plumes and calculate metrics is certainly a source of uncertainty when comparing systems. As an example, for this study, a smaller threshold applied to delineate the Rhône River turbid plume (*e.g.* 2.5 $mg.l^{-1}$) would lightly shift the plume area results to larger values and decrease the differences observed on Fig. 14. The method applied in the present study, based on statistics to assess the SPM concentration "noise" of the background waters, does not rely on *a priori* assumptions on the plume response to forcing, and is only based on ocean color data, then applicable to any coastal systems. The only requirement is to have sufficient cloud-free satellite images over the area.

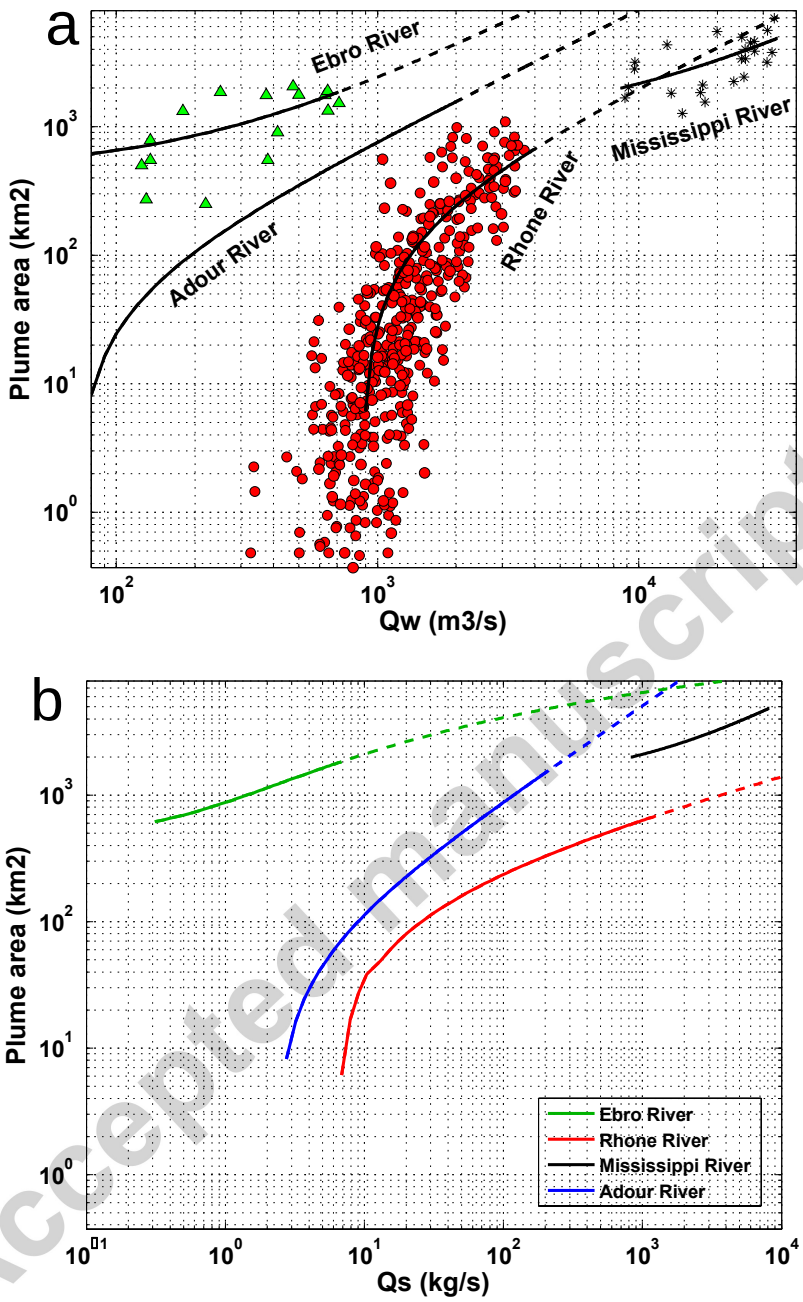

Figure 14: Superposition of plume area to river (a) water discharge and (b) solid discharge relationships for four different systems: the Rhône River (red dots - present study), the Mississippi River (black stars - (Walker, 1996)), the Ebro River (green triangles - (Fernández-Nóvoa et al., 2015)) and the Adour River (Petus et al., 2014). Solid lines represent the different relationships and dashed lines show their extrapolation to higher discharge rates than commonly observed.

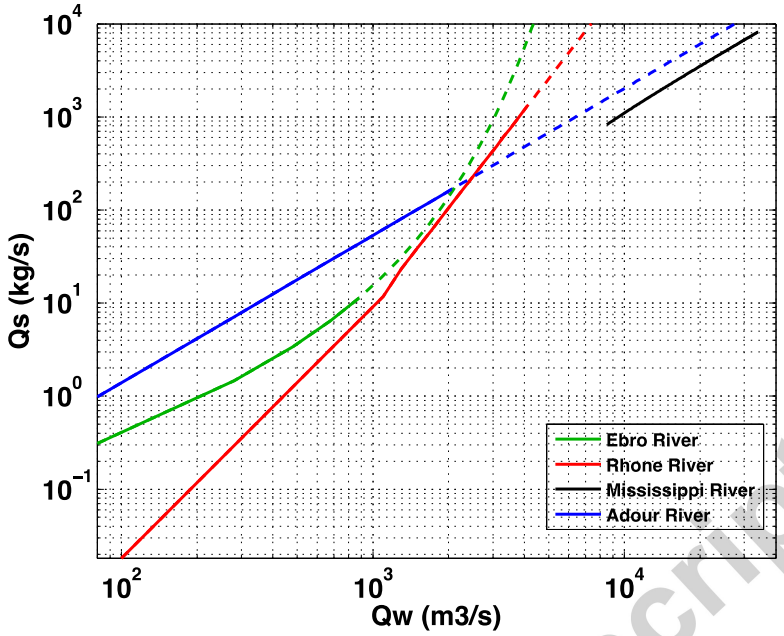

Figure 15: Superposition of suspended sediment discharge (Q_s) to river discharge (Q_w) relationships for four different systems: the Rhône River (red line - (Sadaoui et al., 2016)), the Mississippi River (black line - (Allison et al., 2012)), the Ebro River (green line - (Rovira et al., 2015)) and the Adour River (blue line - (Coynel, 2005)). Solid lines represent the different relationships and dashed lines show their extrapolation to higher discharge rates than commonly observed.

5 Conclusion

An automated processing of ocean color satellite data was developed to isolate the Grand Rhône River turbid plume by a 3 mg.l^{-1} SPM concentration threshold and extract different metrics such as its area of extension, its south-east-westernmost points, its skeleton (proxy of its shape) or its centroid. This tool was applied to the MERIS-300m database covering the 2002-2012 period and more than 800 images were processed. Despite the under-representation of strong SE wind conditions, often related to high river discharges, these images allowed monitoring the area of influence of the Grand Rhône River turbid plume. Results highlighted its seasonal and strong interannual variability, correlated to the Rhône River water discharge. Day-by-day analysis strengthened this correlation and demonstrated that wind orientation also plays a major role on turbid plume's orientation. Offshore winds tend to enhance the current-induced westward plume deflection whereas onshore winds restrain its southern extension and confine it to the coast. The metrics calculated in this study, and especially the centroid and skeleton extraction, are innovative tools to investigate river plume dynamics in various coastal systems. They are also essential in the validation of 3D hydrodynamic and sediment transport models. Remote sensing, autonomous platforms such as gliders, providing complementary observations during flood events (Bourrin et al., 2015; Many et al., 2016), and numerical models will be next combined to estimate sediment fluxes from the Rhône River mouth to the shelf.

Acknowledgements

This work has been done as part of the AMORAD project and received a state aid managed by the Agence Nationale de la Recherche (ANR) under the program Investissements d'avenir (AMORAD-ANR-11-RSNR-0002). We also thank the two anonymous reviewers for their comments and suggestions that significantly improved the manuscript.

References

Allison, M.A., Demas, C.R., Ebersole, B.A., Kleiss, B.A., Little, C.D., Meselhe, E.A., Powell, N.J., Pratt, T.C., Vosburg, B.M., 2012. A water and sediment budget for the lower Mississippi–Atchafalaya River in flood years 2008–2010: Implications for sediment discharge to the oceans and coastal restoration in Louisiana. Journal of Hydrology 432–433, 84-97.

Bourrin, F., Durrieu de Madron, X., 2006. Contribution to the study of coastal rivers and associated prodeltas to sediment supplyi in Gulf of Lions (NW Mediterranean sea). Vie et milieu - Life and Environment 56, 1-8.

Bourrin, F., Many, G., Durrieu de Madron, X., Martín, J., Puig, P., Houpert, L., Testor, P., Kunesch, S., Mahiouz, K., Béguery, L., 2015. Glider monitoring of shelf suspended particle dynamics and transport during storm and flooding conditions. Continental Shelf Research 109, 135-149.

Broche, P., Devenon, J.-L., Forget, P., de Maistre, J.-C., Naudin, J.-J., Cauwet, G., 1998. Experimental study of the Rhone plume. Part I: physics and dynamics. Oceanologica acta 21, 725-738.

Cochrane, J., Kelly, F., 1986. Low ‐ frequency circulation on the Texas ‐ Louisiana continental shelf. Journal of Geophysical Research: Oceans 91, 10645-10659.

Constantin, S., Doxaran, D., Constantinescu, S., 2016. Estimation of water turbidity and analysis of its spatio-temporal variability in the Danube River plume (Black Sea) using MODIS satellite data. Continental Shelf Research 112, 14-30.

Coynel, A., 2005. Erosion mécanique des sols et transferts géochimiques dans le bassin Adour-Garonne. Bordeaux 1.

Demarcq, H., Wald, L., 1984. La dynamique superficielle du panache du Rhône d'après l'imagerie infrarouge satellitaire. Oceanologica Acta 7, 159-162.

Doerffer, R., Schiller, H., 2007. The MERIS Case 2 water algorithm. International Journal of Remote Sensing 28, 517-535.

Doxaran, D., Castaing, P., Lavender, S., 2006. Monitoring the maximum turbidity zone and detecting fine ‐ scale turbidity features in the Gironde estuary using high spatial resolution satellite sensor (SPOT HRV, Landsat ETM+) data. International Journal of Remote Sensing 27, 2303-2321.

Doxaran, D., Froidefond, J.-M., Castaing, P., Babin, M., 2009. Dynamics of the turbidity maximum zone in a macrotidal estuary (the Gironde, France): Observations from field and MODIS satellite data. Estuarine, Coastal and Shelf Science 81, 321-332.

Dufois, F., Garreau, P., Le Hir, P., Forget, P., 2008. Wave- and current-induced bottom shear stress distribution in the Gulf of Lions. Continental Shelf Research 28, 1920-1934.

Dufois, F., Verney, R., Le Hir, P., Dumas, F., Charmasson, S., 2014. Impact of winter storms on sediment erosion in the Rhone River prodelta and fate of sediment in the Gulf of Lions (North Western Mediterranean Sea). Continental Shelf Research 72, 57-72.

Ekman, V.W., 1905. On the influence of the earth's rotation on ocean currents. Ark. Mat. Astron. Fys. 2, 1-53.

Estournel, C., Durrieu de Madron, X., Marsaleix, P., Auclair, F., Julliand, C., Vehil, R., 2003. Observation and modeling of the winter coastal oceanic circulation in the Gulf of Lion under wind conditions influenced by the continental orography (FETCH experiment). Journal of Geophysical Research 108.

Estournel, C., Kondrachoff, V., Marsaleix, P., Vehil, R., 1997. The plume of the Rhone: numerical simulation and remote sensing. Continental Shelf Research 17, 899-924.

Fanget, A.-S., Bassetti, M.A., Arnaud, M., Chiffoleau, J.F., Cossa, D., Goineau, A., Fontanier, C., Buscail, R., Jouet, G., Maillet, G.M., 2013. Historical evolution and extreme climate events during the last 400years on the Rhone prodelta (NW Mediterranean). Marine Geology 346, 375-391.

Fernández-Nóvoa, D., Mendes, R., deCastro, M., Dias, J.M., Sánchez-Arcilla, A., Gómez-Gesteira, M., 2015. Analysis of the influence of river discharge and wind on the Ebro turbid plume using MODIS-Aqua and MODIS-Terra data. Journal of Marine Systems 142, 40-46.

Font, J., Salat, J., Julià, A., 1990. Marine circulation along the Ebro continental margin. Marine Geology 95, 165-177.

Forget, P., Devenon, J.L., De Maistre, J.C., Broche, P., Leveau, M., 1990. VHF remote sensing for mapping river plume circulation. Geophysical Research Letters 17, 1097-1100.

Garcia, D., 2010. Robust smoothing of gridded data in one and higher dimensions with missing values. Computational statistics & data analysis 54, 1167-1178.

Gernez, P., Barillé, L., Lerouxel, A., Mazeran, C., Lucas, A., Doxaran, D., 2014. Remote sensing of suspended particulate matter in turbid oyster‐farming ecosystems. Journal of Geophysical Research: Oceans 119, 7277-7294.

Gohin, F., 2011. Annual cycles of chlorophyll-a, non-algal suspended particulate matter, and turbidity observed from space and in-situ in coastal waters. Ocean Science 7, 705.

Gohin, F., Loyer, S., Lunven, M., Labry, C., Froidefond, J.-M., Delmas, D., Huret, M., Herbland, A., 2005. Satellite-derived parameters for biological modelling in coastal waters: Illustration over the eastern continental shelf of the Bay of Biscay. Remote Sensing of Environment 95, 29-46.

Güttler, F.N., Niculescu, S., Gohin, F., 2013. Turbidity retrieval and monitoring of Danube Delta waters using multi-sensor optical remote sensing data: An integrated view from the delta plain lakes to the western–northwestern Black Sea coastal zone. Remote Sensing of Environment 132, 86-101.

Hudson, A.S., Talke, S.A., Jay, D.A., 2016. Using Satellite Observations to Characterize the Response of Estuarine Turbidity Maxima to External Forcing. Estuaries and Coasts, 1-16.

Lorthiois, T., Doxaran, D., Chami, M., 2012. Daily and seasonal dynamics of suspended particles in the Rhône River plume based on remote sensing and field optical measurements. Geo-Marine Letters 32, 89-101.

Maillet, G.M., Vella, C., Berné, S., Friend, P.L., Amos, C.L., Fleury, T.J., Normand, A., 2006. Morphological changes and sedimentary processes induced by the December 2003 flood event at the present mouth of the Grand Rhône River (southern France). Marine Geology 234, 159-177.

Many, G., Bourrin, F., de Madron, X.D., Pairaud, I., Gangloff, A., Doxaran, D., Ody, A., Verney, R., Menniti, C., Le Berre, D., 2016. Particle assemblage characterization in the Rhone river ROFI. Journal of Marine Systems.

Marsaleix, P., Estournel, C., Kondrachoff, V., Vehil, R., 1998. A numerical study of the formation of the Rhône River plume. Journal of Marine Systems 14, 99-115.

Mestres, M., Sierra, J.P., Sánchez-Arcilla, A., González del Río, J., Wolf, T., Rodríguez, A., Ouillon, S., 2003. Modelling of the Ebro River plume. Validation with field observations. Scientia Marina 67, 379-391.

Millot, C., 1990. The Gulf of Lions' hydrodynamics. Continental Shelf Research 10, 885-894.

Millot, C., Taupier-Letage, I., 2005. Circulation in the Mediterranean sea, The Mediterranean Sea. Springer, pp. 29-66.

Müller, D., Krasemann, H., Brewin, R.J.W., Brockmann, C., Deschamps, P.-Y., Doerffer, R., Fomferra, N., Franz, B.A., Grant, M.G., Groom, S.B., Mélin, F., Platt, T., Regner, P., Sathyendranath, S., Steinmetz, F., Swinton, J., 2015. The Ocean Colour Climate Change Initiative: I. A methodology for assessing atmospheric correction processors based on in-situ measurements. Remote Sensing of Environment 162, 242-256.

Murray, S.P., 1972. Observations on wind, tidal, and density-driven currents in the vicinity of the Mississippi River delta. Shelf Sediment Transport, Dowden, Hutchinson and Ross, Stroudsburg, PA, 127-142.

Nechad, B., Ruddick, K.G., Park, Y., 2010. Calibration and validation of a generic multisensor algorithm for mapping of total suspended matter in turbid waters. Remote Sensing of Environment 114, 854-866.

Ody, A., Doxaran, D., Vanhellemont, Q., Nechad, B., Novoa, S., Many, G., Bourrin, F., Verney, R., Pairaud, I., Gentili, B., 2016. Potential of High Spatial and Temporal Ocean Color Satellite Data to Study the Dynamics of Suspended Particles in a Micro-Tidal River Plume. Remote Sensing 8, 245.

Petus, C., Chust, G., Gohin, F., Doxaran, D., Froidefond, J.-M., Sagarminaga, Y., 2010. Estimating turbidity and total suspended matter in the Adour River plume (South Bay of Biscay) using MODIS 250-m imagery. Continental Shelf Research 30, 379-392.

Petus, C., Marieu, V., Novoa, S., Chust, G., Bruneau, N., Froidefond, J.-M., 2014. Monitoring spatio-temporal variability of the Adour River turbid plume (Bay of Biscay, France) with MODIS 250-m imagery. Continental Shelf Research 74, 35-49.

Radakovitch, O., Charmasson, S., Arnaud, M., Bouisset, P., 1999. 210Pb and Caesium Accumulation in the Rhône Delta Sediments. Estuarine, Coastal and Shelf Science 48, 77-92.

Roditis, J.-C., Pont, D., 1993. Dynamiques fluviales et milieux de sédimentation du Rhône à l'amont immédiat de son delta. Méditerranée 78, 5-18.

Rolland, B., 2006. Transfert des radionucléides artificiels par voie fluviale: conséquences sur les stocks sédimentaires rhodaniens et les exports vers la Méditerranée. Th ese de doctorat, 280.

Rouse, L.J., Coleman, J.M., 1976. Circulation observations in the Louisiana bight using LANDSAT imagery. Remote Sensing of Environment 5, 55-66.

Roussiez, V., Aloisi, J.-C., Monaco, A., Ludwig, W., 2005. Early muddy deposits along the Gulf of Lions shoreline: A key for a better understanding of land-to-sea transfer of sediments and associated pollutant fluxes. Marine Geology 222-223, 345-358.

Rovira, A., Ibáñez, C., Martín-Vide, J.P., 2015. Suspended sediment load at the lowermost Ebro River (Catalonia, Spain). Quaternary International 388, 188-198.

Sadaoui, M., Ludwig, W., Bourrin, F., Raimbault, P., 2016. Controls, budgets and variability of riverine sediment fluxes to the Gulf of Lions (NW Mediterranean Sea). Journal of Hydrology 540, 1002-1015.

Schroeder, W.W., Dinnel, S.P., Wiseman, W.J., Merrell, W.J., 1987. Circulation patterns inferred from the movement of detached buoys in the eastern Gulf of Mexico. Continental Shelf Research 7, 883-894.

Stoichev, T., Amouroux, D., Wasserman, J.C., Point, D., De Diego, A., Bareille, G., Donard, O.F.X., 2004. Dynamics of mercury species in surface sediments of a macrotidal estuarine–coastal system (Adour River, Bay of Biscay). Estuarine, Coastal and Shelf Science 59, 511-521.

Walker, N.D., 1994. Satellite-based assessment of the Mississippi River discharge plume's spatial structure and temporal variability. OCS Study MMS 94, 0053.

Walker, N.D., 1996. Satellite assessment of Mississippi River plume variability: Causes and predictability. Remote Sensing of Environment 58, 21-35.

Walker, N.D., Wiseman Jr, W.J., Rouse Jr, L.J., Babin, A., 2005. Effects of river discharge, wind stress, and slope eddies on circulation and the satellite-observed structure of the Mississippi River plume. Journal of Coastal Research, 1228-1244.

Wang, G., Garcia, D., Liu, Y., De Jeu, R., Dolman, A.J., 2012. A three-dimensional gap filling method for large geophysical datasets: Application to global satellite soil moisture observations. Environmental Modelling & Software 30, 139-142.

Warrick, J.A., Fong, D.A., 2004. Dispersal scaling from the world's rivers. Geophysical Research Letters 31.

Wieliczka, D.M., Weng, S., Querry, M.R., 1989. Wedge shaped cell for highly absorbent liquids: infrared optical constants of water. Applied optics 28, 1714-1719.